Preprint Title	Damage characteristic of aluminum nanorod under hypervelocity impact
Authors	Yong-Chao Wu, Jian-Li Shao and Haifei Zhan
Publication Date	07 Okt 2019
Article Type	Full Research Paper
ORCID® iDs	Yong-Chao Wu - https://orcid.org/0000-0003-4228-3398

Damage characteristic of aluminum nanorod under hypervelocity impact

Yong-Chao Wu[1], Jian-Li Shao[*1] and Haifei Zhan[2]

Address: [1]State Key Laboratory of Explosion Science and Technology, Beijing Institute of Technology, Beijing 100081, China and [2]School of Chemistry, Physics and Mechanical Engineering, Queensland University of Technology, Brisbane QLD 4001, Australia

Email: Jian-Li Shao - shao_jianli@bit.edu.cn

[*] Corresponding author

Abstract

Understanding the dynamic behavior of materials under hypervelocity impact is of great importance to develop new materials or structures for protective applications. The present work gives insight into the damage characteristic of aluminum nanorod under hypervelocity impact based on atomistic simulations. First of all, the propagation of impact wave is found to experience a rapid decaying because of its release from the side surface, which leads to a complex three-dimensional stress wave and two tension regions inside the nanorod. The damage mode under this tension state is found to be very different from the classical spallation. Due to the interaction of two release waves from the side and end surfaces, a temporary spall damage is observed and its initial tensile strength is close to that of bulk material. However, that early spall damage does not develop into a complete spall fracture. More importantly, all generated voids are found to be closed eventually after their coalescence. Furthermore, the mass continues expanding outward from the impact plane and finally causes a radial annular fragmentation. The annular fragmentation shows a clear crystalline direction dependence for low impact velocities. The number and the size of final fragments are found to follow a power law relationship for all impact velocities.

1

Keywords

nanorod, hypervelocity impact, damage, atomistic simulation

Introduction

Spallation is a typical failure case in studying the mechanisms those underlie and govern material strength, and spallation is essentially attributed to the void nucleation, growth and coalescence for ductile metals[1]. In the past decades, it has attracted abundant experimental, theoretical and computational researches. In experiments, plate impact[2-4] and laser shock [5-7] techniques are commonly used to detect the spall damage with high strain rates ranging about from 10^5 to $10^{10} s^{-1}$. Previous studies have shown that the spallation strength depends on not only the shock pulse[3] and strain rate[6], but also the microstructure of material, such as crystal orientation[2] and grain size[7]. However, the required spatiotemporal resolutions for a comprehensive understanding of the void nucleation and growth is still prohibitive for state-of-the-art experimental techniques. In terms of theoretical research, many empirical models have been developed to describe the spallation based on experimental data and numerical simulations[8-10]. For instance, Czarnota *et al.*[10] reproduced the experimental results for different thickness flyers and different impact velocities very well by using Weibull function to describe the stress distribution of void nucleation. Of course, the dynamic damage in materials under extreme condition is often coupled with complex deformation, heat generation and even phase change. Thus, it is very hard to consider all the influence factors at the same time in constructing a theoretical damage constitutive model, and there is still no general spall criterion. Correspondingly, numerical simulation methods at different physical scales have been developed to probe the damage dynamics of materials. Such as the finite element methods[11,12] within the framework of the continuum mechanics, the recently developed quasi-coarse-grained dynamics[13,14] and molecular dynamics (MD) simulations.

At present, MD simulation has become a resourceful tool in studying various deformation mechanisms in materials at atomistic level. Recent MD researches[15-22] have shown many microstructure effects related to spallation, such as the grain size, anisotropy and intrinsic defects. For exam-

2

ple, it is found that when grain size decreases continuously to lower than 20 nm, the yield strength of materials will change from an increasing trend to a decreasing trend, triggering the so-called inverse Hall-Petch effect[7,23-25]. Remington *et al.*[7] found that the spallation in nanocrystalline tantalum is primarily intergranular under relatively low strain rate deformation and hence the effect of grain size is inverse Hall-Petch regulation. In practice, the dynamic response of nanomaterials can exhibit more diverse characteristics because of the strong surface and crystal orientation effects. The properties of the compressed surface are strongly dependent on a range of impact parameters, including impact velocity, material of incident particle, crystal orientation and temperature, etc. For example, Lee *et al.*[26] conducted a microscopic ballistic test to study the shock responses of nanocomposites and prominently show the orientation-dependence of energy dissipation. Pogorelko *et al.*[27] investigated the impact process of copper nanoparticle with aluminum surface and obtain the optimal range of temperature and collision velocity for producing high-quality layers of copper on the aluminum surface. These effects are becoming more and more concerned in relative application fields, such as the aerosol deposition and cold spraying[28], space debris, etc.

Overall, the specific research on the dynamic mechanism of nanoscale materials is still in its infancy. In this regard, this work aims to exploit the dynamic damage characteristic in nanorod under planar impact loading. Here, lightweight face-centered cubic aluminum is selected, since aluminum and aluminum hybrid matrix composites are promising candidates for a mass of structural applications attributed to their excellent mechanical properties[29,30]. Based on the simulation results, the decaying in stress propagation, void nucleation and evolution, as well as fragmentation power law are all revealed. The structure of manuscript is as follows: Simulation details are introduced in Section 2, results and discussion are presented in Section 3, and finally summaries are drawn in Section 4.

Simulation details

The empirical potential or force field is the physical basis of MD simulations, which determines the accuracy and authenticity of results. Here, we choose the embedded atom method (EAM) potential improved by Zhakhovskii *et al.*[31], which is suitable to simulate the behavior of aluminum crystal under strong dynamic compression and tension. The initial configuration is a single crystal aluminum nanorod with 1,360,329 atoms, whose diameter is $60a$ and length is $120a$. The left $30a$ is set as a flyer region and the last $90a$ as a target region, as shown in Fig.1. Here a is the lattice constant and $a = 0.4032$ nm. The x, y and z axes are along [100], [010] and [001] orientations, respectively. Our MD simulations are performed with the open-source LAMMPS[32] code. To obtain a stable nanorod structure, the system is firstly relaxed by energy minimization with conjugate gradient method, and then fully equilibrated in isothermal isobaric ensemble (NPT) with Nosé-Hoover thermostat until it comes to minimum energy state. The relaxation temperature is set to 50 K to reduce thermal noise to some extent. The impact processes are simulated in micro-canonical ensemble (NVE) and free boundaries are set in all the three directions. The impact velocity U_f varies from 4 km/s to 7 km/s, which is added on the flyer region along the z direction. The time step in all simulations is 1 fs.
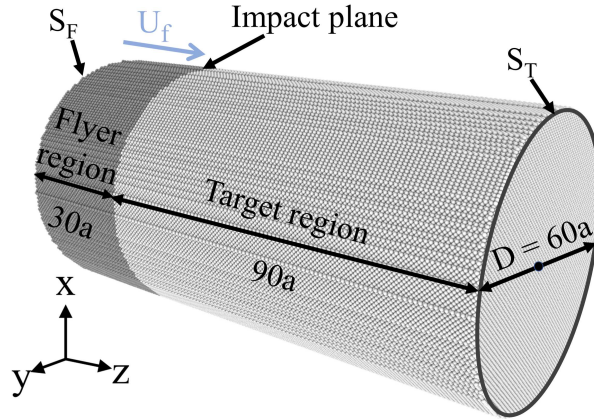

Figure 1: Three-dimensional view of the single crystal aluminum nanorod. The diameter is $60a$ and length is $120a$. The left $30a$ is set as the flyer region with impact velocity U_f and the other $90a$ is the target region. S_F and S_T denote the left and right end surfaces.

Based on the atomic stress and microstructure analysis, we discuss the shock wave propagation,

4

⁹¹ tensile strength, damage evolution and fragmentation. The atomic stress is calculated according to

⁹² virial formula[33]. And the shock pressure is obtained by averaging the stress components in the

⁹³ x, y and z directions, i.e., $P = -(\sigma_{xx} + \sigma_{yy} + \sigma_{zz})/3$. The atomic visualizations are performed by

⁹⁴ Ovito(the Open Visualization Tool)[34], and specifically, the void surface morphology is visualized

⁹⁵ with the construct surface mesh tool(Ovito)[35], which can also provide the value of surface areas.

⁹⁶ The number and size of clusters during fragmentation process are obtained with cluster analysis

⁹⁷ tool(Ovito).

Results and discussion

The decaying property of impact wave

¹⁰⁰ Above of all, we compare our simulations with the shock Hugoniot relations. The pressure peaks

¹⁰¹ from our direct simulations are 40-98 GPa at the impact velocity 4-7 km/s, which agree well with

¹⁰² the Hugoniot pressure calculated from $P_H = \rho_0 u_s u_p$. Here, ρ_0 is the initial sample density, u_s is the

¹⁰³ shock wave velocity and u_p is the particle velocity. These results indicate that the current impact

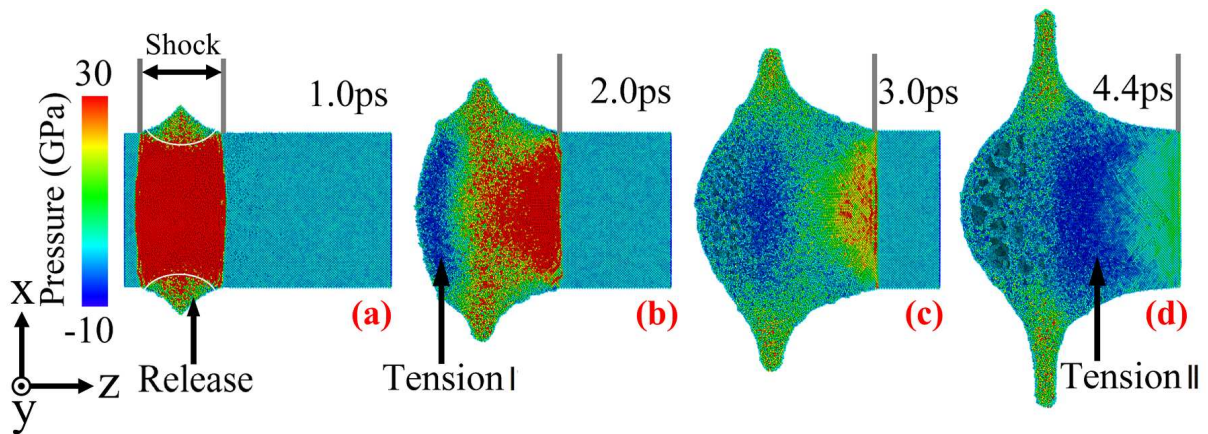¹⁰⁴ scenario is almost an one-dimensional planar impact at the early stage.

Figure 2: Views of atomic stress distribution at different moments (a-d) after impact (U_f = 7km/s). The release of shock wave at side surface is marked by white arcs (a), which changes the shocked stress distribution significantly. And interestingly, two different tension regions (b and d) can be observed inside the nanorod. The shock front is illustrated by gray lines.

¹⁰⁵ The time evolution of microscopic pressure distributions is presented in Fig.2 by considering the

case of $U_f = 7$ km/s. We firstly observe the formation of double shock waves after impact. Also, the expansion of impact plane and the pressure release from the side surface already become distinct at about 1.0 ps (Fig.2 (a)). At 2.0 ps (Fig.2 (b)), there appears the first tension region (Tension I) near the left end surface, caused by the interaction between the two release waves from left end and side surfaces. This early stage is similar to the typical spallation. The void nucleation inside Tension I region occurs between 3.0 to 4.4 ps, as shown in Fig.2 (c) and (d). However, the planar wave turns into a complex three-dimensional waves with time going. And we observe another tension region (Tension II) in the target region. Apparently, the Tension II region is distinctly larger than the Tension I region, and the shock pressure peak is already significantly reduced when it arrives at the right end surface. Thus, the damage state in target region is relatively weak.
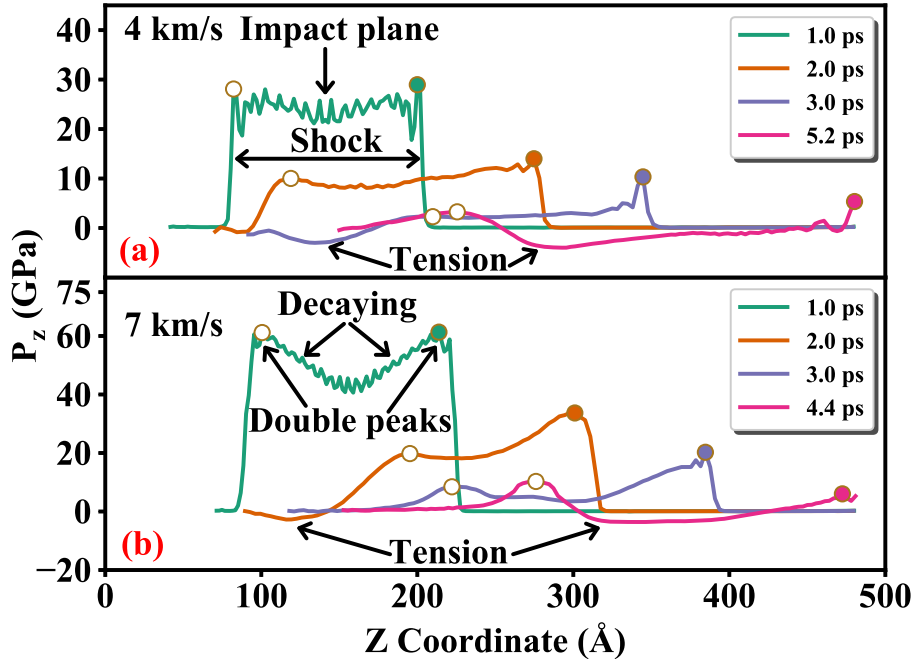

Figure 3: Time evolution of pressure profile for (a) $U_f = 4$ km/s and (b) 7 km/s, respectively. P_z means the average pressure of each bin along z direction.

Based on the above dynamic process, we examine the pressure profiles for $U_f = 4$ km/s and 7 km/s by estimating the average pressure of each bin($\sim$0.5 a) along z direction, and the results are shown in Fig.3. Due to the strong surface release effect, the peak pressure will experience an evident decaying. Our simulations show that the pressure peak changes from 40(98) GPa to 30(60) GPa for

$U_f = 4(7)$ km/s within 1.0 ps. As illustrated in Fig.2, there forms a radial release wave propagates inwards and meantime results in a dramatic expansion of the impact plane. Note that, the decaying spontaneously renders a unique double peaks phenomenon. And the stress wave reflection from the left end surface causes the Tension I in the flyer region. Moreover, with the propagation of different release waves, we observe the formation of Tension II, whose tension stress peak(~ 4 GPa) is slightly larger than that in Tension I(~ 3 GPa). Eventually, the peak pressure reduces to less than 10 GPa when the stress wave spreads to the right end surface in both cases of $U_f = 4$ km/s and 7 km/s.
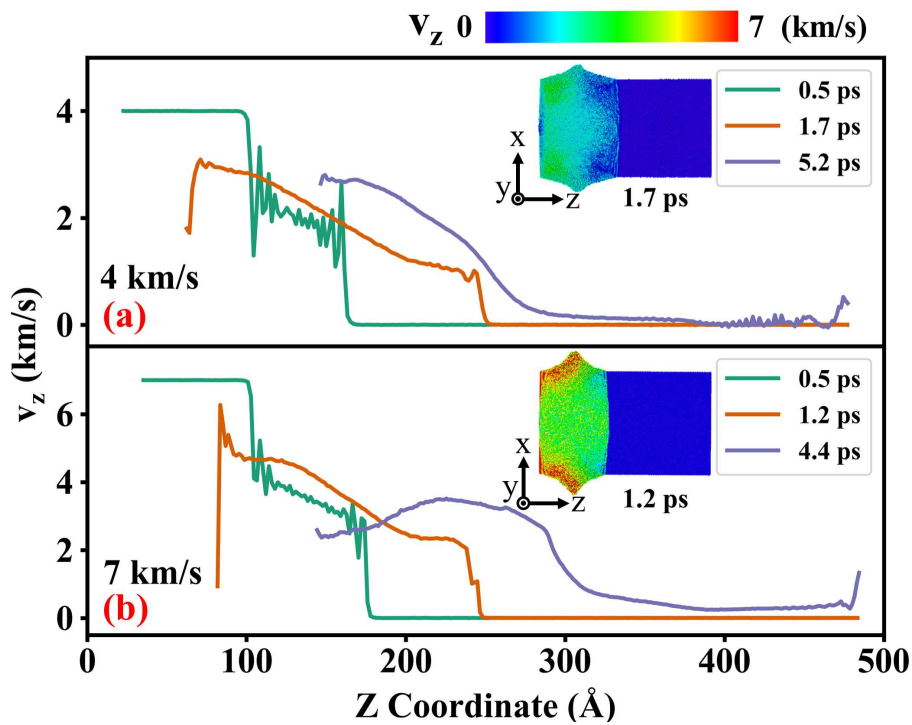

Figure 4: Time evolution of velocity profile for (a) $U_f = 4$ km/s and (b) 7 km/s, respectively. The two microscopic views are sliced from center axis.

Further, we present in Fig.4 the axial velocity profiles at different times $U_f = 4$ km/s and 7 km/s, respectively. As described above, the release from the side surface will affect the impact wave profiles significantly. Here, we find that the particle velocity in shocked region seems to follow a linear distribution in the early stage, and its profile becomes irregular and form a complex three-dimensional distribution with the impact wave propagation.

Surface velocity history and tensile strength

Tensile strength is crucial to measure dynamic properties of materials. Spallation is a typical failure case in studying the mechanisms, which occurs where the two strong release waves meet. The entire spall process in ductile metal consists of the nucleation, growth, and coalescence of voids[1]. And the maximum of tensile stress during the spall process is regarded as the spall strength. In practice, the tensile strength is often deduced from the free surface velocity history based on acoustic approximation[1], since the *in situ* detection of spall stress is extremely difficult.
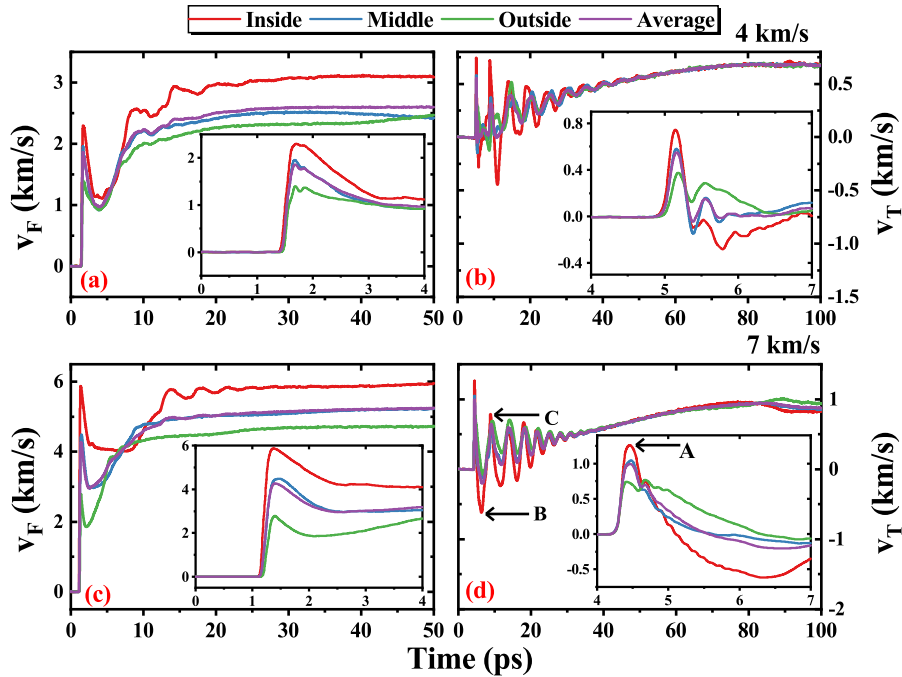

Figure 5: Time evolution of two end surface velocities. v_F (a and c) and v_T (b and d) represent the left and right end surface velocities along z direction respectively. The points A, B and C denote the velocity peak and valley at the early time.

In Fig.5, we present velocity history of the two end surfaces, i. e. the left (v_F) and right (v_T) surface velocities, by taking the cases of the U_f = 4 km/s and 7 km/s. Considering the severe deformation in the end surface during the impact process, the end surfaces are divided into three parts, including the inside part with $r \leq 6$ nm, the middle part with $6 < r \leq 10$ nm and the outside part with $r > 10$ nm. For both left and right end surfaces, the surface experiences a change from peak to valley. Nevertheless, there is remarkable difference between the two end surfaces during the following

8

process. For left end surface S_F, a remarkable pullback with a period of ~ 10 ps is observed, which is followed by a velocity plateau (since the flyer region rapidly melts on the shock release and thus there hardly form the stress wave reflection, as shown in Fig.5 (a) and Fig.5 (c)). For right end surface S_T, its velocity history can be characterized into three distinct stages (Fig.5 (b) and Fig.5 (d)), i. e. oscillated acceleration, smooth acceleration and final velocity plateau, which reflect various evolutions of inside damage. After being shocked, the velocity of S_T is found to decay from A to B rapidly with the interactions of release waves from the side and end surfaces, and then rises to C, resulting from that the new voids surfaces reflect the release wave into the compression wave. The compression wave also leads to the voids coalescence at the target region. In other words, the oscillation includes both the void nucleation and the wave reflection from the material end and side surfaces. After all the voids disappear (at around 13.0 ps), this kind of oscillation decreases and the acceleration becomes smooth. Finally, as the energy dissipation of waves and degree of material breakage increase, the velocity of S_T increases gradually and reaches a velocity plateau. The spall strength from surface and bulk are both analyzed here. As expected, the velocity in the central region of the end surface experiences the most significant change, so we choose the inside part to estimate the tensile strength with the acoustic approximation[1] according to Eq.1. Meanwhile, the tensile strength from bulk is determined by Eq.2 with the maximum tensile stress during impact.

$$\sigma_s = 0.5\rho_0 c \Delta v_s \tag{1}$$

$$\sigma_s = Max[stress(z,t)] \tag{2}$$

where ρ_0 is the initial sample density, and c denotes the sound speed in the sample. In fact, there exist three tensile stress peaks at different positions in the nanorod, i. e. vicinity of both end surfaces and the middle of the target region, respectively. The computational tensile strength results for different impact velocities U_f are presented in Fig.6. As is seen, the tensile stress from the right end surface σ_{s2} shows a large deviation between the examined impact velocity between 4 km/s and

7 km/s. This is mainly due to the inappropriateness of acoustic approximation under strong impact, which has been discussed in previous articles [36,37]. The tensile stresses in other regions, including the vicinity of S_F (σ_{s3}), middle of the target region (σ_{s4}), and the vicinity of S_T (σ_{s5}), are in the range of 3 GP and 6 GPa, and they follow a general relationship as $\sigma_{s5} > \sigma_{s4} > \sigma_{s3}$. The flyer rapidly transforms from solid into liquid state after impact, thus the tensile strength shown in Fig.6 is the minimum. The peak pressure near S_T is less than 10 GPa (Fig. 3), and σ_{s5} has the maximum value as expected.
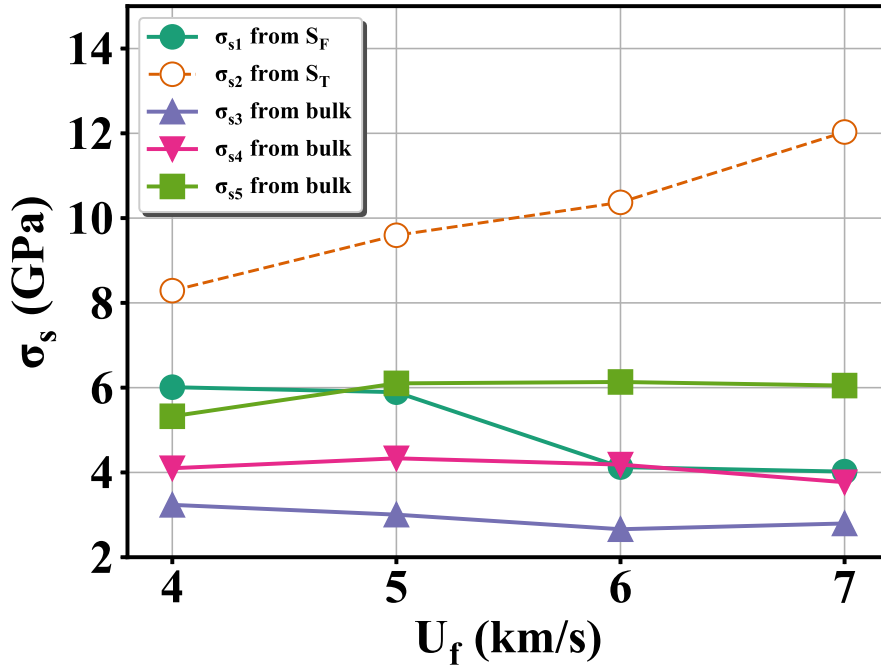

Figure 6: Tensile strength of sample from bulk and end surface for different impact velocities. σ_{s1} and σ_{s2} are calculated from S_F and S_T respectively, σ_{s3}, σ_{s4} and σ_{s5} are taken from the vicinity of S_F, middle of target and the vicinity of S_T, respectively.

Void nucleation, evolution and closure

We further explore the detailed damage evolution inside the nanorod. As discussed above, the material will form voids due to the interaction between the radial and axial release waves. Here, we choose $U_f = 5$ km/s and 7 km/s cases to demonstrate the void nucleation and evolution process, as illustrated in Fig.7 (a) and Fig.7 (b), respectively. The void evolution can be readily divided into four stages, i.e., nucleation, growth, coalescence and closure. At the early time, the nucleation of

10

voids is observed and these small voids mainly appear along [110] and [1$\bar{1}$0] orientations, due to the strong surface effects and crystal orientations effects. Compared with U_f = 5km/s, more voids are generated and they appear earlier under the higher impact velocity of U_f = 7km/s. The size and the number of the voids increase gradually until 4.5 ps. Thereafter, voids coalesce begins, which leads to the formation of bigger voids. More importantly, these voids do not develop into entire spall fracture eventually like macroscopic impact. We find that the rapid expansion of impact region will limit the growth of voids and even absorb them. After the complete disappearance of voids in the target region, the voids in the flyer region at the same time transform into a very large void. Such big void is unable to support the extrusion at the melting state and gradually shrink and close completely at 13.0 ps.
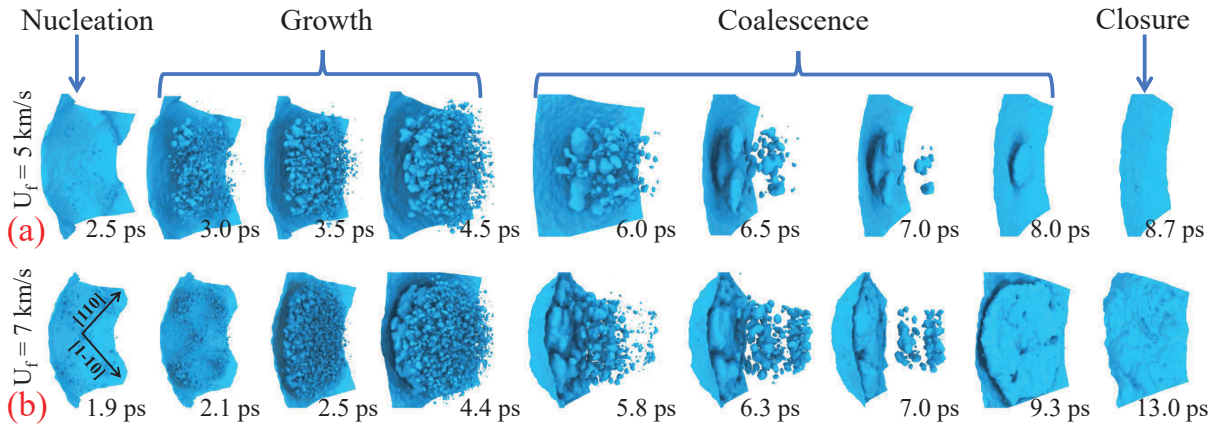

Figure 7: Microscopic views of void evolution for: (a) U_f = 5 km/s; and (b) 7 km/s. For (b), the microscopic views at the time of 4.4, 6.3 and 9.3 ps correspond to the points A, B and C in Fig.5, respectively.

To further understand the void evolution, Fig.8 compares the surface areas of total voids(S_{voids}) between U_f = 5 km/s and 7 km/s. As is seen, the surface area starts to increase at 2.5 ps and 1.9 ps for U_f = 5 km/s and 7 km/s, respectively, indicating the nucleation of voids. With continuing simulation, the surface area increases significantly, and reaches the maximum at 4.5 ps and 4.4 ps for U_f = 5 km/s and 7 km/s, respectively. Specifically, the maximum voids surface area under U_f =7 km/s is almost two times of that under U_f = 5 km/s. After that, it decreases remarkably due to the voids coalescence. It is noted that there is a clear inflection on the surface area profile during the decreasing period, which is caused by the formation of bigger voids. The surface area decreases to

11

zero eventually, due to the closure of voids. Compared with $U_f = 5$ km/s, the voids appear earlier and last for longer under the higher impact velocity of $U_f = 7$ km/s.
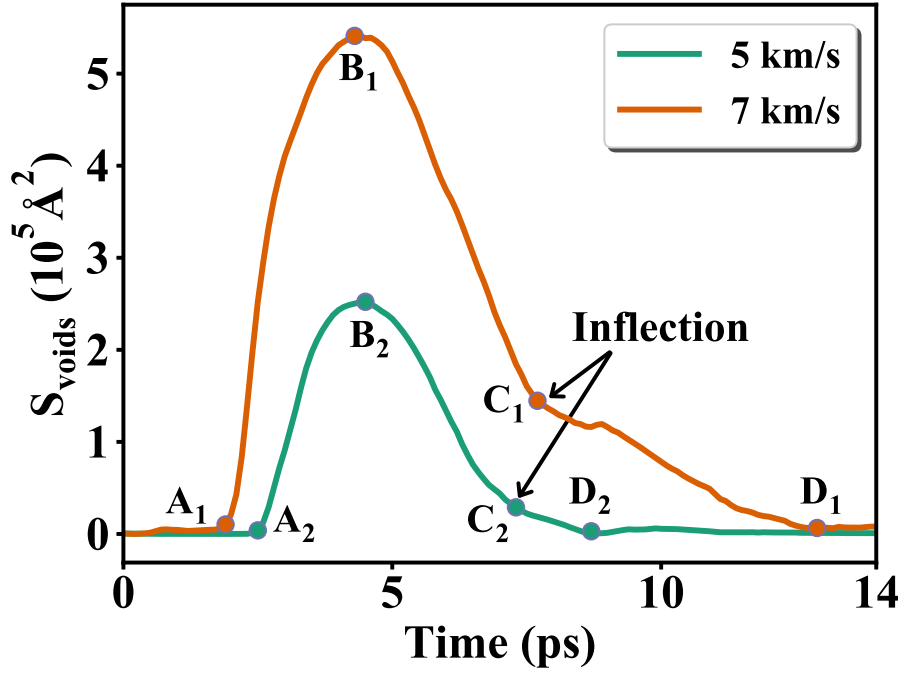

Figure 8: Variation of the surface areas of total voids with time for the cases of $U_f = 5$ km/s and 7 km/s, respectively. A, B, C, D represent the nucleation, maximal surface area, coalescence, and complete closing of voids, respectively. An obvious inflection on the curves can be seen, implying that the convergent holes begin to close.

Radial expansion and fragmentation

The evolution of radial average velocity ($v_r = \sqrt{v_x^2 + v_y^2}$) of impact plane is presented in Fig.9, which provide important information at the early stage of radial expansion. Here, a cylindrical section on the impact plane with a thickness of $10a$ is selected to analyze the impact process for the cases of $U_f = 4$ km/s and 7 km/s, respectively. To note that atoms at the edge of the impact layer first gain velocity rather than atoms in the center region due to the strong side surface release effect. As shown in Fig.9 (a) and Fig.9 (b), the radial velocity at the time of 0.5 ps is almost a constant from the center to a radial distance of around 10 nm, and it increases sharply nearly the edge. With further simulation, the radial velocity of the central area increase, and results in a gradual increasing profile. Interestingly, the radial velocity profile shows a distinct discontinuity point at the

position of the initial radius (highlighted by the dashed magenta lines in Fig.9 (a) and Fig.9 (b)).

As expected, the impact layer expands faster under $U_f = 7$ km/s and the velocity of the edge atoms
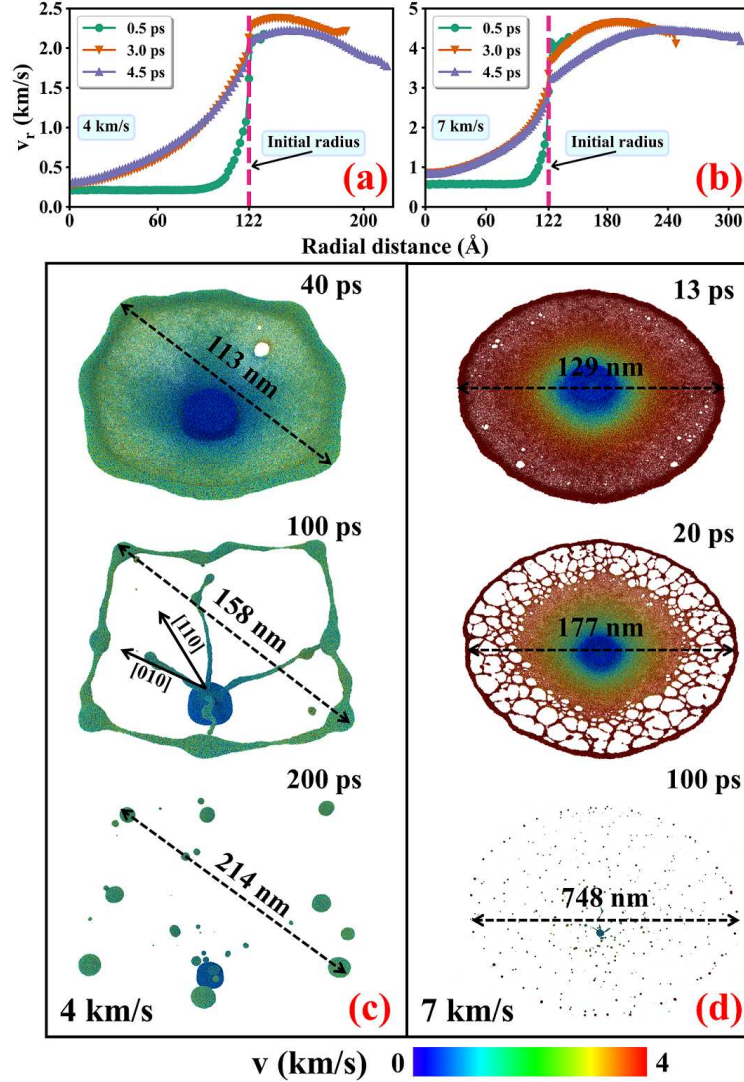
is higher than the atoms at center.

Figure 9: The radial velocity distributions in the impact plane for (a) $U_f = 4$ km/s and (b) 7 km/s at different moments. The microscopic views demonstrate the fragmentation process and for better visualization those views have been scaled differently. The results for $U_f = 4$ km/s show an evident orientation dependence and the results for $U_f = 7$ km/s seem to be a ring breakup. And the former has very limited and larger clusters, than the latter. The atoms are colored by their average speed v.

The impact plane continues to expand and forms many fragments. To analysis the structural evolu-

tion, we decompose the sample into disconnected clusters (that contains a number of atoms) based

on a cutoff radius that equals to the lattice constant. The typical pictures of cluster evolution, in-

cluding formation, expansion and fragmentation under the conditions of U_f = 4 km/s and 7 km/s are shown in Fig.9 (c) and Fig.9 (d). According to Fig.9 (c) under the velocity of U_f =4 km/s, the front part of the target region remains in a solid state during the impact process, while the other regions are like in a melt state. Due to the rapid outward expansion, fragmentation appears at the vicinity of the edges of the impact layer (due to the different expansion rates). The debris spread from the center to the periphery and exhibit distinct shapes (at the time of 100 ps in Fig.9 (c)). It is interesting to note that the formed fragments or debris are along the [110] and [010] crystalline directions. Under high impact velocity (U_f =7 km/s, Fig.9 (d)), similar fragmentation process is observed. The difference is much earlier separation between the central area and the edges is observed (at 20 ps). Due to the high kinetic energy, the sample eventually decomposes into a larger number of small clusters.

We further estimate the number and size of clusters using the approach as utilized in literature[38, 39]. The distribution of number and size of clusters under different impact velocities U_f exhibits similar features. As shown in Fig.10, the size distribution manifests a remarkable power laws of follow form:

$$N_c(N_p) \propto N_p{}^k \tag{3}$$

where N_p is the number of atoms in each cluster and N_c is the number of clusters corresponding to N_p. The solid line in Fig.10 represents the power law between N_c and N_p, which is fitted from the final state of different impact processes. We use the green dash line for the case of U_f = 4 km/s, since the number of clusters here is too small. $|k|$ seems to increase with the increase of U_f, which increases from 1.49 to 1.87 when U_f increases from 5 km/s to 7 km/s. Notice that $N_p < 1000$ is neglected for the fitting, which is considered as insignificant in the fragmentation process. The distribution has similarity with ejecta size distribution[39] and the results can reveal some regulations of clusters evolution during hypervelocity impact at nanoscale.
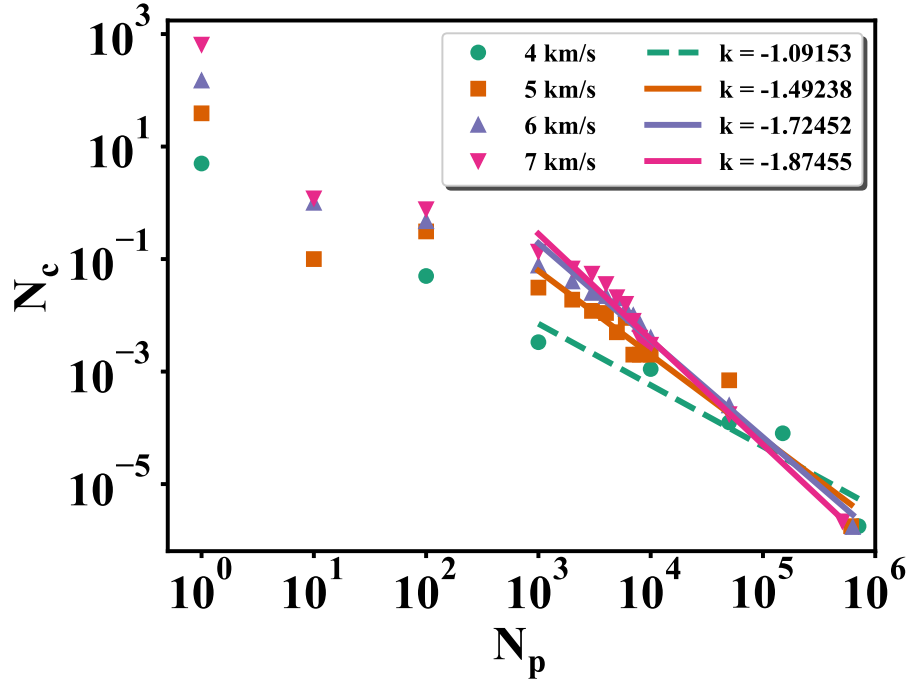
14

Figure 10: Relationship between the number of atoms in each cluster N_p and the corresponding number of clusters N_c at different impact velocities U_f.

Summary

In this work, we conduct MD simulations to investigate the damage characteristic of single crystal aluminum nanorod under hypervelocity impact. The simulation results demonstrate some interesting dynamic properties. During the propagation process, the impact pressure experiences a rapid decaying due to its release from the side surface, which is reflected by the pressure and velocity profiles along the axial direction. The interaction of impact wave and its release wave from side and end surfaces result in a complex three-dimensional stress state. Two tension regions in the nanorod are formed, which lead to the nucleation of voids. The evolution of voids can lead to the oscillation of flyer free surface velocity to some extent and the tensile strength of nanorod is similar with that of bulk aluminum from our simulations. However, all these voids are temporary and they will close after they grow and coalesce, therefore no complete spall fracture occurs ultimately. Such observation is due to the increasing new surface release effect limits the expansion of voids and the velocity gradient can easily facilitate the voids to collapse at melting state. Besides, the void nucleation is preferably along [110] and [1$\bar{1}$0]. Additionally, it is found that the cluster for-

15

mation under low impact velocity is found to exhibit an apparent orientation dependence related to the early damage evolution, and at final state each cluster is close to a sphere due to the surface tension. Specifically, the cluster number is found to follow a power law relationship with the cluster size.

Acknowledgements

References

1. Antoun, T.; Curran, D. R.; Razorenov, S. V.; Seaman, L.; Kanel, G. I.; Utkin, A. V. *Spall Fracture*; Shock Wave and High Pressure Phenomena; Springer Science & Business Media, 2003; doi:https://doi.org/10.1007/b97226.

2. Turley, W. D.; Fensin, S. J.; Hixson, R. S.; Jones, D. R.; La Lone, B. M.; Stevens, G. D.; Thomas, S. A.; Veeser, L. R. *Journal of Applied Physics* **2018**, *123* (5), 055102. doi:10.1063/1.5012267.

3. Kanel, G. I. *International Journal of Fracture* **2010**, *163* (1), 173–191. doi:10.1007/s10704-009-9438-0.

4. Jiang, Z. J.; He, J. Y.; Wang, H. Y.; Zhang, H. S.; Lu, Z. P.; Dai, L. H. *Materials Research Letters* **2016**, *4* (4), 226–232. doi:10.1080/21663831.2016.1191554.

5. Milathianaki, D.; Boutet, S.; Williams, G. J.; Higginbotham, A.; Ratner, D.; Gleason, A. E.; Messerschmidt, M.; Seibert, M. M.; Swift, D. C.; Hering, P.; Robinson, J.; White, W. E.; Wark, J. S. *Science* **2013**, *342* (6155), 220–3. doi:10.1126/science.1239566.

6. Remington, T. P.; Remington, B. A.; Hahn, E. N.; Meyers, M. A. *Materials Science and Engineering: A* **2017**, *688*, 429–458. doi:10.1016/j.msea.2017.01.114.

7. Remington, T. P.; Hahn, E. N.; Zhao, S.; Flanagan, R.; Mertens, J. C. E.; Sabbaghian-rad, S.; Langdon, T. G.; Wehrenberg, C. E.; Maddox, B. R.; Swift, D. C.; Remington, B. A.; Chawla, N.; Meyers, M. A. *Acta Materialia* **2018**, *158*, 313–329. doi:10.1016/j.actamat.2018.07.048.

8. Johnson, J. N. *Journal of Applied Physics* **1981**, *52* (4), 2812–2825. doi:10.1063/1.329011.

9. Curran, D.; Seaman, L.; Shockey, D. *Physics Reports* **1987**, *147* (5), 253 –388. doi:https://doi.org/10.1016/0370-1573(87)90049-4.

10. Czarnota, C.; Jacques, N.; Mercier, S.; Molinari, A. *Journal of the Mechanics and Physics of Solids* **2008**, *56* (4), 1624–1650. doi:10.1016/j.jmps.2007.07.017.

11. Xie, W.; Alizadeh-Dehkharghani, A.; Chen, Q.; Champagne, V. K.; Wang, X.; Nardi, A. T.; Kooi, S.; Müftü, S.; Lee, J. H. *Scientific reports* **2017**, *7* (1), 5073. doi:10.1038/s41598-017-05104-7.

12. Chen, X. D.; Chan, A. H. C. *International Journal of Impact Engineering* **2018**, *112*, 15–29. doi:10.1016/j.ijimpeng.2017.10.007.

13. Dongare, A. M. *Philosophical Magazine* **2014**, *94* (34), 3877–3897. doi:10.1080/14786435.2014.961992.

14. Agarwal, G.; Valisetty, R. R.; Namburu, R. R.; Rajendran, A. M.; Dongare, A. M. *Scientific Reports* **2017**, *7* (1), 12376. doi:10.1038/s41598-017-12340-4.

15. Lin, L.; Zeng, X. *Eng Fract Mech* **2015**, *142*, 50–63. doi:10.1016/j.engfracmech.2015.05.039.

16. Dongare, A. M.; Rajendran, A. M.; LaMattina, B.; Zikry, M. A.; Brenner, D. W. *Phys. Rev. B* **2009**, *80*, 104108. doi:10.1103/PhysRevB.80.104108.

17. Branicio, P. S.; Nakano, A.; Kalia, R. K.; Vashishta, P. *International Journal of Plasticity* **2013**, *51*, 122–131. doi:10.1016/j.ijplas.2013.06.002.

18. Hahn, E. N.; Fensin, S. J.; Germann, T. C.; Gray, G. T. *Acta Materialia* **2018**, *159*, 241–248. doi:10.1016/j.actamat.2018.07.073.

19. Xiang, M. Z.; Cui, J. Z.; Yang, Y. T.; Liao, Y.; Wang, K.; Chen, Y.; Chen, J. *International Journal of Plasticity* **2017**, *97*, 24–45. doi:10.1016/j.ijplas.2017.05.008.

20. Mayer, A. E.; Mayer, P. N. *International Journal of Mechanical Sciences* **2019**, *157-158*, 816–832. doi:https://doi.org/10.1016/j.ijmecsci.2019.05.023.

21. Mayer, A. E.; Ebel, A. A. *Journal of Applied Physics* **2016**, *120* (16), 165903. doi:10.1063/1.4966555.

22. Xia, K.; Zhan, H.; Ji, A.; Shao, J.; Gu, Y.; Li, Z. *Beilstein Journal of Nanotechnology* **2019**, *10*, 1588–1595. doi:10.3762/bjnano.10.154.

23. Xu, W. W.; Dávila, L. P. *Materials Science and Engineering: A* **2017**, *692*, 90–94. doi:10.1016/j.msea.2017.03.065.

24. Xu, W. W.; Dávila, L. P. *Materials Science and Engineering: A* **2018**, *710*, 413–418. doi:10.1016/j.msea.2017.10.021.

25. Wilkerson, J. W.; Ramesh, K. T. *Phys Rev Lett* **2016**, *117* (21), 215503. doi:10.1103/PhysRevLett.117.215503.

26. Lee, J. H.; Veysset, D.; Singer, J. P.; Retsch, M.; Saini, G.; Pezeril, T.; Nelson, K. A.; Thomas, E. L. *Nat Commun* **2012**, *3*, 1164. doi:10.1038/ncomms2166.

27. Pogorelko, V. V.; Mayer, A. E.; Krasnikov, V. S. *Applied Surface Science* **2016**, *390*, 289–302. doi:10.1016/j.apsusc.2016.08.067.

28. Assadi, H.; Kreye, H.; Gärtner, F.; Klassen, T. *Acta Materialia* **2016**, *116*, 382–407. doi:10.1016/j.actamat.2016.06.034.

29. Bodunrin, M. O.; Alaneme, K. K.; Chown, L. H. *Journal of Materials Research and Technology* **2015**, *4* (4), 434–445. doi:https://doi.org/10.1016/j.jmrt.2015.05.003.

30. Shin, S. E.; Choi, H. J.; Shin, J. H.; Bae, D. H. *Carbon* **2015**, *82*, 143–151. doi:10.1016/j.carbon.2014.10.044.

31. Zhakhovskii, V. V.; Inogamov, N. A.; Petrov, Y. V.; Ashitkov, S. I.; Nishihara, K. *Applied Surface Science* **2009**, *255* (24), 9592–9596. doi:https://doi.org/10.1016/j.apsusc.2009.04.082. Proceedings of the Sixth International Conference onPhoto-Excited Processes and Applications(6-ICPEPA)

32. Plimpton, S. *Journal of Computational Physics* **1995**, *117* (1), 1–19. doi:https://doi.org/10.1006/jcph.1995.1039.

33. Thompson, A. P.; Plimpton, S. J.; Mattson, W. *The Journal of Chemical Physics* **2009**, *131* (15), 154107. doi:10.1063/1.3245303.

34. Stukowski, A. *Modelling and Simulation in Materials Science and Engineering* **2009**, *18* (1), 015012. doi:10.1088/0965-0393/18/1/015012.

35. Stukowski, A. *JOM* **2014**, *66* (3), 399–407. doi:10.1007/s11837-013-0827-5.

36. Luo, S. N.; An, Q.; Germann, T. C.; Han, L. B. *Journal of Applied Physics* **2009**, *106* (1), 013502. doi:10.1063/1.3158062.

37. Shao, J. L.; Wang, P.; He, A. M.; Zhang, R.; Qin, C. S. *Journal of Applied Physics* **2013**, *114* (17), 173501. doi:10.1063/1.4828709.

38. Durand, O.; Soulard, L. *Journal of Applied Physics* **2012**, *111* (4), 044901. doi:10.1063/1.3684978.

39. He, A. M.; Wang, P.; Shao, J. L. *Computational Materials Science* **2015**, *98*, 271–277. doi:10.1016/j.commatsci.2014.11.020.